Journal of Thermal Science Vol.31, No.5 (2022) 1709−1722

https://doi.org/10.1007/s11630-022-1658-x **Article ID: 1003-2169(2022)05-1709-14**

Aerodynamic Comparison between Increasing Cascade Pitch and Turning Angle in the Highly-Loaded Design

ZHOU Xun[1#*], XUE Xingxu[1,2#], DU Xin[1], LUO Lei[1], WANG Songtao[1]

1. School of Energy Science and Engineering, Harbin Institute of Technology, Harbin 150001, China
2. Science and Technology on Diesel Engine Turbocharging Laboratory, China North Engine Research Institute, Tianjin 300270, China

Abstract: Theoretical and numerical study was carried out based on a linear turbine cascade (the Basic cascade) to compare the influences of the increased cascade pitch and turning angle in this paper. On one hand, the two highly-loaded designs both reduced the stability of flow field through enhancing adverse pressure gradient and span-wise pressure gradient of the fluid near suction surface. Therefore, the two highly-loaded designs would both result in thicker boundary layer and stronger secondary flow, so the secondary loss would be increased and more difficult to suppress in the highly-loaded cascades. On the other hand, the two highly-loaded designs showed different influences on the pitch-wise migration of the fluid near the endwall (cross flow) because of the different load enhancing mechanisms. In other words, the increased cascade pitch (TCx highly-loaded design) would delay the pitch-wise migration of the horseshoe vortex because of the increased channel width, while the increased turning angle (Turn highly-loaded design) would do the opposite because of the increased pitch-wise pressure gradient. As a result, the enhancement of the interaction between the fluid near the suction surface and the cross flow would be much stronger in the Turn highly-loaded design than the TCx highly-loaded design, and the span-wise developing tendencies of vortexes and fluid near the suction surface would show much stronger enhancing tendency in the former than the latter.

Keywords: linear turbine cascade, highly-loaded design, secondary flow, enhancing pattern, enhancing mechanism

1. Introduction

The endwall secondary flow, which was the result of the wall viscous shear, would lead to stronger mixing process and higher endwall loss in turbomachinery [1]. In detail, Wang's team [2] has presented that the vortexes can obviously strengthen the mixing processes in linear turbine cascades by experiment, while Langston [3] indicated that the dissipation in turbomachinery would be promoted by both thicker boundary layer and stronger vortex structure. Therefore, it is necessary to suppress the development of secondary flow in turbomachinery [4, 5].

The highly-loaded design, which can reduce the total number of blades [6] by raising cascade pitch or turning angle, would offer notable advantages in increasing the thrust-weight ratio of turbomachinery by reducing its self-weight [7, 8]. However, studies also had showed that the highly-loaded design can also lead to more

---

#These authors contributed equally to the work and should be regarded as co-first authors.

AE: KAN Xiaoxu

Received: May 09, 2020

Corresponding author: ZHOU Xun

E-mail: zhouxun@hit.edu.cn

Nomenclature

C	Chord
C_o	Circulation load coefficient
$Cp\mathrm{s}$	Static pressure coefficient
$Cp\mathrm{t}$	Mass average total pressure loss coefficient
C_Q	Normalized Q coefficient
H	Blade height
k	Adiabatic exponent
Ma	Mach number
$\dot{m}$	Mass flow
P	Pressure
Q	Q criterion
Re	Reynolds number
S	Arc length
S_F	Strain rate
SP	Static pressure
T	Pitch
v	Velocity
W_F	Vorticity
x	Axial-wise
Y	Equivalent constant of channel width
y	Pitch-wise
y^+	Dimensionless distance from wall
z	Span-wise
Z_w	Zweifel load coefficient
α	Practical flow angle
β	Designed flow angle
Δ	Absolute deviation
δ	Relative deviation
μ	Dynamic viscosity
υ	Kinematic viscosity
ξ	Mass average energy loss coefficient
ρ	Density
Subscript	
1	Inlet plane
2	Outlet plane
2D	Two-dimensional
3D	Three-dimensional
s	Static value
t	Total value
Superscript	
—	Equivalent constant
^	Area average value
Abbreviation	
CV	Corner vortex
DVS	Distance between vortex and suction surface
HV	Horseshoe vortex
IAVS	Included angle between vortex axis and suction normal
PL-HV	Pressure leg of horseshoe vortex
PS	Pressure surface
PV	Passage vortex
RANS	Reynolds Average Navier-Stokes
SS	Suction surface
SV	Shedding vortex
WV	Wall vortex

complicated secondary flow structure [9]. Therefore, the secondary loss would be increased [10] and more difficult to suppress [11]. For instance, Tan's team [12] had studied the influence of the blade bowing design in a turbine cascade with large turning angle. However, the study gained only insignificant improvements though the flow field was obviously affected. Besides, Chen's team [13] had indicated the higher turning angle would reduce the optional range of the bowing angle in compressor. Moreover, Ingram's team had [14] proved large scale separation and increased endwall loss was caused by a non-axisymmetric endwall in the Durham cascade.

Therefore, it was necessary to study the universal enhancing patterns and enhancing mechanisms of the secondary flow, on considering to improve the effectiveness of the commonly used of control methods (such as the blade bowing design and the non-axisymmetric endwall design) in highly-loaded cascades. Due to the differences in research ideas, however, it would be rather difficult to find out a previous study which could perfectly satisfy the universality and usability requirements in this study. For instance, Weiss's team [15] and Lyall [16] had both studied the influence of the loading distribution on secondary flow. Due to the affections of the different geometrical and aerodynamical conditions, however, the conclusions they had gained were almost the opposite to each other. Besides, Lyall's team [17] and Sangston's team [18] had studied the influence of the stagger angle near the endwall and gained similar conclusions. However, their conclusions were too difficult to be applied in improving the effectiveness of the commonly used control methods.

The surface static pressure gradient was always regarded as the bridge [19, 20] between the geometrical and aerodynamical characteristics, because it is the major driving force [21] of secondary flow. For instance, Zess's team [22] indicated that the leading edge fillet would reduce the span-wise pressure gradient near the leading edge to suppress the pressure leg of horseshoe vortex

(PL-HV). Lyall's team [17] and Sangston's team [23] believed that the adjusted stagger angle near the endwall would reduce the adverse pressure gradient near the pressure surface (PS) to weaken the inlet boundary and PL-HV. Ingram's team [24] and Torre's team [25] suggested that the non-axisymmetric endwall would adjust the pitch-wise pressure gradient near the endwall region to suppress the cross flow. Tan's team [26] and Han's team [27] had indicated the pressure gradient distribution near the suction surface (SS) would be influenced by the bowing design, so the development of the passage vortex (PV), corner vortex (CV), wall vortex (WV) and shedding vortex (SV) would be obviously affected. Therefore, it is reasonable to study the enhancement mechanism by analyzing the variation of the pressure distribution.

In this paper, the influences of the increased cascade pitch and turning angle were compared by both numerical simulations and theoretical derivations. The similar secondary flow enhancing patterns between the two highly-loaded designs were mainly discussed based on the weakened flow field stability and enhanced secondary pressure gradients, while the different enhancing patterns were mainly discussed based on their different influences on the pitch-wise migrating tendencies of the cross flow. Moreover, the differently influenced cross flows were further studied based on the different load enhancing mechanisms between the two highly-loaded designs.

Generally, the numerical methods and results were introduced in Section 2 and Section 3, respectively. Section 2 presented the definitions of the parameters in Section 2.1, and introduced the details of geometry in Section 2.2, and introduced the 2.3 Simulation scheme and validation based on Ref. [28] in Section 2.3. In Section 3, the usability of the adjusted cascades was verified in Section 3.1. Then, the enhancing patterns were preliminarily discussed and analyzed between the two highly-loaded designs in Section 3.2. Finally, the mechanism of the different enhancing patterns was further discussed in Section 3.3. Moreover, the pressure gradient would be regarded as negative if the fluid is driven to the endwall and PS along the blade surface and endwall, respectively.

2. Numerical Methods

In this paper, the highly-loaded design is carried out with the help of the Blade-Editor. The Blade-Editor is a blade-modeling software, of which all rights are reserved by Engine and Aerodynamics Research Center (EARC). Moreover, structural meshes are generated by NUMECA Autogird, while the RANS method of the ANSYS CFX software was applied in the simulation. Moreover, this study and Ref. [28] belong to the same series, and the numerical methods are inevitably similar between them. Therefore, some of the contents are simplified without influencing the readability of a paper, with the purpose to avoid the suspicion of plagiarism.

2.1 Parameter definitions

The Zweifel load coefficient [29, 30] as well as Circulation load coefficient [11, 31] is applied to quantify the load of cascade in this study, and their definitions are:

$$Z_{\mathrm{w}} = \left(\oint P_{\mathrm{s}} \cdot \mathrm{d}x\right) \Big/ \left[Cx \cdot \left(P_{1,\mathrm{s}} - P_{2,\mathrm{s}}\right)\right] \tag{1}$$

$$C_{\mathrm{o}} = \left(\oint v_{\mathrm{s}} \cdot \mathrm{d}S\right) \Big/ \left(v_2 - S_0\right) \tag{2}$$

where Cx is the axial chord; P_{s} is the measured static pressure; $P_{1,\mathrm{s}}$ is the inlet static pressure; $P_{2,\mathrm{s}}$ is the outlet static pressure; S_0 is the length of SS; S is measured arc length; v_{s} is the measured velocity near SS; v_2 is the outlet velocity.

The normalized Q criterion [32, 33] coefficient (C_Q) [34] is applied to ensure the vortex structure in this study, and the definitions of C_Q and Q are:

$$C_Q = \sqrt{Q/Q_{\max}} \qquad (Q > 0) \tag{3}$$

$$\begin{aligned} Q &= 0.5 \cdot \left(W_{\mathrm{F}}{}^2 - S_{\mathrm{F}}{}^2\right) \\ &= 0.5 \cdot \left[0.25 \cdot \left(\frac{\partial v_i}{\partial x_j} - \frac{\partial v_j}{\partial x_i}\right)^2 - 0.25 \cdot \left(\frac{\partial v_i}{\partial x_j} + \frac{\partial v_j}{\partial x_i}\right)^2\right] \end{aligned} \tag{4}$$

where $Q_{\max}$ is the maximum Q; S_{F} is the fluid strain rate; W_{F} is the fluid vorticity; i and j are two axis directions; v_i is the velocity component along i-axis; v_j is the velocity component along i-axis; $\partial v_i/\partial x_j$ is the gradient of v_i along j-axis; $\partial v_j/\partial x_i$ is the gradient of v_j along i-axis.

The mass average total pressure loss coefficient [35, 36] and the mass average energy loss coefficient [37, 38] are applied to measure the loss in this study, and their definitions are:

$$Cp\mathrm{t} = \left(P_{1,\mathrm{t}} - P_{\mathrm{t}}\right) / \left(P_{2,\mathrm{t}} - P_{2,\mathrm{s}}\right) \tag{5}$$

$$\xi = \frac{\left(\dfrac{P_{2,\mathrm{s}}}{P_{\mathrm{t}}}\right)^{(k-1)/k} - \left(\dfrac{P_{2,\mathrm{s}}}{P_{1,\mathrm{t}}}\right)^{(k-1)/k}}{1 - \left(\dfrac{P_{2,\mathrm{s}}}{P_{1,\mathrm{t}}}\right)^{(k-1)/k}} \tag{6}$$

where P_{t} is the measured total pressure; $P_{1,\mathrm{t}}$ is the inlet total pressure at the midspan; $P_{2,\mathrm{t}}$ is the outlet total pressure; k is the fluid adiabatic exponent.

The static pressure coefficient [39, 40] is applied to measure the static pressure distribution in this study, and its definition is:

$$Cp\mathrm{s} = \left(P_{\mathrm{s}} - P_{2,\mathrm{s}}\right) / \left(P_{1,\mathrm{t}} - P_{2,\mathrm{s}}\right) \tag{7}$$

The Reynolds number [41, 42] is applied to ensure the comparability between the cascades. In this study, the outlet Reynolds number is calculated based on the axial chord, and the definition is:

$$Re_2 = \left(\rho \cdot v_2 \cdot Cx\right) / \mu \tag{8}$$

where μ is the fluid dynamic viscosity; ρ is the fluid density.

2.2 Physical models

According to the discussion in Ref. [28], the coordinate system and measuring planes are presented in Fig. 1 based on the three-dimensional (3D) geometry of the Basic cascade. As shown, the blade is placed at $0.00x_{Cx}$ to $1.00x_{Cx}$; three measuring planes are uniformly distributed in $0.10z_H$ to $0.50z_H$, while nine are uniformly distributed in $-0.10x_{Cx}$ to $1.10x_{Cx}$.

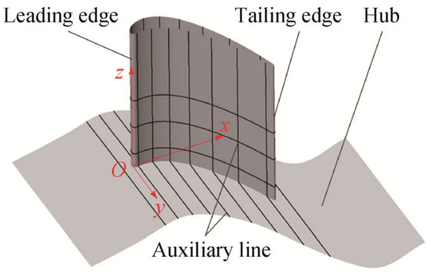

Fig. 1 The coordinate system and measuring planes

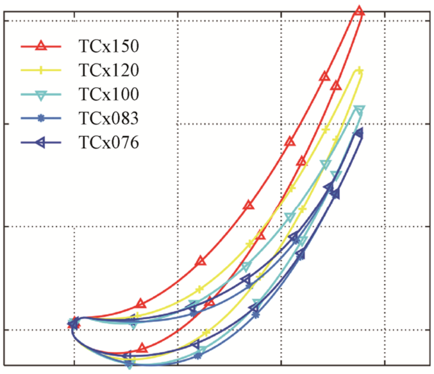

(a) TCx cases

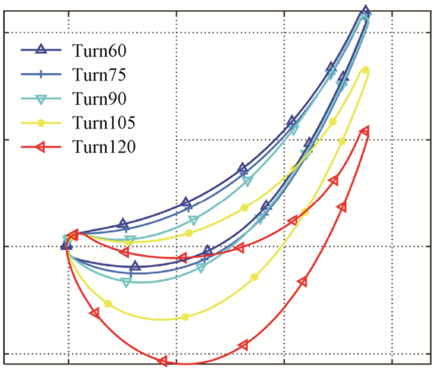

(b) Turn cases

Fig. 2 The two-dimensional (2D) blade profiles of the Turn cases and TCx cases

The two-dimensional (2D) blade profiles are presented in Fig. 2. Generally, the main difference among the TCx profiles is the cascade pitch, while it is the turning angle in the Turn profiles. Specifically, the TCx100 profile/cascade and the Turn100 profile/cascade are totally the same profile/cascade (Basic profile/cascade).

Key design parameters for straight cascades are shown in Table 1, while the designed inlet flow angle (β_1) and outlet flow angle (β_2) are both measured by the axial chord. Generally, Cx, blade height (H) and β_2 are not varied in both groups. In detail, β_1 is varied from 0° to 60° with fixed cascade pitch (T) in the Turn cascades, while T/Cx is varied from 0.76 to 1.50 with fixed β_1 during the TCx cascades.

Table 1 The key design parameters for all cascades

Case	T/Cx	β_1/(°)	β_2/(°)	β_1–β_2/(°)	H/Cx
Turn120	1.00	60.00	–62.03	122.03	2.21
Turn105	1.00	45.00	–62.03	107.03	2.21
Turn90	1.00	29.20	–62.03	91.23	2.21
Turn75	1.00	15.00	–62.03	77.03	2.21
Turn60	1.00	0.00	–62.03	62.03	2.21
TCx150	1.50	29.20	–62.03	91.23	2.21
TCx120	1.20	29.20	–62.03	91.23	2.21
TCx100	1.00	29.20	–62.03	91.23	2.21
TCx083	0.83	29.20	–62.03	91.23	2.21
TCx076	0.76	29.20	–62.03	91.23	2.21

2.3 Simulation scheme and validation

The simulation medium is air (ideal gas), and the total temperature at the inlet plane is selected as 1086 K in this study. Moreover, Blanco's team [43] had indicated the thickness of inlet endwall boundary layer would influence the radial migration tendency of the inlet flow near the blade, so the different thicknesses had led to significantly different secondary flow structures and overall losses as a result. Therefore, a nonuniform inlet total pressure distribution is applied, while $P_{2,s}$ is about $0.74P_{1,t}$ in this study. Moreover, the lowest total pressure at the inlet plane is $0.95P_{1,t}$, so the energy loss coefficient would be increased by the inlet boundary layer. The detailed distribution is shown in Fig. 3.

According to the discussion in Ref. [28], a grid strategy, of which the number of node is about 1.5 million, was chosen for the simulations. In detail, the O4H mesh is locally refined near the solid walls, while the area average y^+ is about 1. The mesh sensitivity is validated based on the total pressure loss coefficient (Cpt) and flow angle (β_2) at the outlet plane, while it shows that the grid strategy with 2 million nodes will only lead to negligibly slight variations less than 0.001 and 0.015°, respectively. Moreover, Fig. 4 shows the the selected grid strategy based on the Basic cascade.

Simulation and experimental results of the modelling Basic cascade are compared to ensure the usability of commonly used turbulence models and the reliability of the numerical method. The experiment is carried out in 129 low-speed plane cascade wind tunnel and measurement system [44], which belongs to Engine & Aerodynamics Research Center (EARC) in Harbin Institute of Technology (HIT). The measurement is carried out mainly by the calibrated five-hole pressure probe, 9116 pressure scanner and oil-trace flow visualization system.

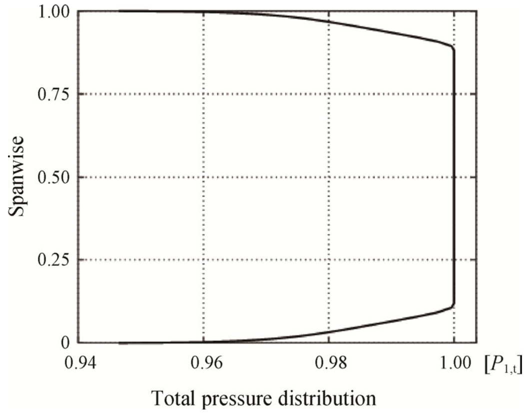

Fig. 3 The distribution of the inlet total pressure, reprinted from Ref. [28] , copyright 2020, with permission from SAGE

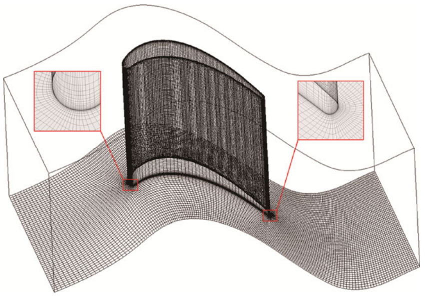

Fig. 4 The grid visualization results of the Basic cascade

As had been shown in Ref. [28], the SST γ-θ turbulence model is selected in this study. Generally, it presents that the SST γ-θ turbulence model is much better than the k-w, k-ε, SST and BSL γ-θ turbulence models in predicting the span-wise distribution of loss coefficient and flow angle at $1.12x_{Cx}$ plane, especially at $0.00z_H$ to $0.05z_H$ and $0.20z_H$ to $0.50z_H$. Moreover, Ref. [28] also proved that the current scheme matches the experiment well in predicting the development tendencies of the secondary flow structures, for good consistencies between the experimental oil trace and simulated limiting streamlines are shown.

With the purpose of prove the credibility of the simulation, Fig. 5 presents the numerical and experimental results of Cpt at $1.12x_{Cx}$. As a result, it shows that the numerical simulation can provide accurate predictions of the total pressure loss distribution on measuring section. In detail, the experiment shows that PV, SV and the corner vortex (CV) lead to several high-loss regions near endwall, while the cascade wake causes a high-loss region which is almost constant along span-wise near the midspan. Obviously, the current numerical method is still not perfect and shows a few minor errors. For instance, the simulated high-loss region near PV is a little nearer to the midspan than the experiment, while some predictive errors can be found in the rectangle at about $0.08z_H$. However, the current simulation has provided generally accurate predictions in the loss distribution of the main channel as well as the high-loss regions that are resulting from PV, SV, CV near the endwall and the cascade wake near the midspan.

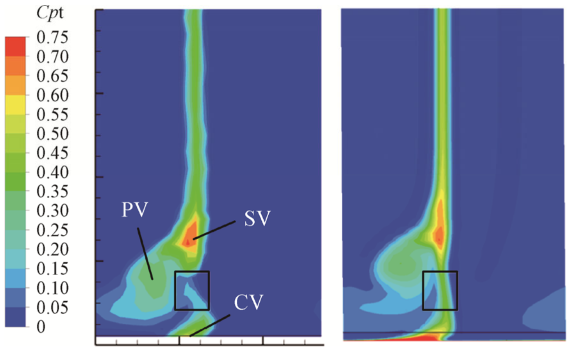

Fig. 5 Comparisons of the Cpt at $1.12x_{Cx}$ between the simulation and experiment, reprinted from Ref. [28] , copyright 2020, with permission from SAGE

Therefore, the simulated results in this paper should be expected to be reliable.

3. Results and Discussion

3.1 Verification of the load adjustment

Table 2 presents groups of the 2D and 3D parameters to confirm that the loading adjustment is suitable for the following study.

The load distribution. Table 2 shows that distributions of cascade loads are suitable for the following study. On one hand, Table 2 shows that the alteration trends of Z_w and C_o are similar during the load adjusting progress, so the variation of cascade load that reflected by Z_w and C_o are reliable in this study. On the other hand, Table 2 shows the two groups of cascades have similar load distributions, while the maximum loads are both approximately twice of the minimum values. Therefore, the load distributions of the cascades are suitable for the following within-group and between-group comparisons.

The comparability between profiles. Table 2 proves that the comparability among the 2D profiles is pretty good. In detail, the relative deviations of outlet flow angle ($\delta|\alpha_{2D,2}|$) and mass flow ($\delta\hat{m}_{2D}$) are both much lower than 1%, which reflects that the flow through capacity and flow turning capacity are both have very slight differences from the Basic profile (named as TCx100 and Turn90 in two groups).

The comparability between cascades. Table 2 shows that the highly-loaded designs would have much stronger influences on the 3D flow field than 2D, so further verification would be carried out to ensure that this situation is caused by the enhanced secondary flow. Generally, Table 2 shows that the deviations caused by the highly-loaded design are generally acceptable in the cascades except the Turn120 cascade. In detail, the Turn120 cascade has much lower outlet mass average Mach number (Ma_2) and Reynolds number (Re_2), while 3D relative deviations of outlet mass flow ($\delta\hat{m}_{3D}$) and flow angle ($\delta|\alpha_{3D,2}|$) are both several times bigger than the other cascades. Therefore, it is necessary to ensure the increased deviations in the Turn120 cascade would not affect the comparability between the Turn120 cascade and Basic cascade, so further confirmations would be carried out in Section 3.2 to ensure the increased deviations are not caused by unwanted disturbances such as large separation.

3.2 Comparative study of the enhancing patterns

3.2.1 Comparative study based on simulated data

Table 3 presents the parameters that would assist the evaluation of secondary flow. On considering the main differences between the 3D and 2D results should be caused by the secondary flow [3], it is reasonable to measure the energy loss coefficient caused by the secondary flow by the differences between the 3D and 2D mass average energy loss coefficients ($\xi_{3D}-\xi_{2D}$). Similarly, $|\alpha_{3D,2}|-|\alpha_{2D,2}|$, which is the difference between the 3D and 2D absolute mass average outlet flow angles, can reflect the influence of the secondary flow on the fluid turning angle. Therefore, Table 3 generally shows that the higher load would lead to enhanced secondary flow, while the influences of the increased load are not totally the same between the two groups.

Moreover, it should also be noted that the variation of the cascade pitch would influence mass flow of a single channel. Therefore, the loss coefficients of TCx cases should have been reduced by the increased mass flow. For instance, Table 3 shows the ratios of ξ_{2D} and $\xi_{3D}-\xi_{2D}$ between the TCx150 cascade, TCx120 cascade and Basic cascade are 239:202:218 and 325:285:247, respectively. On considering the ratio of the single channel mass flow between the three cascades is 15:12:10, the ratios of the single channel profile loss and endwall loss between the three cascades are 359:242:218 and 488:342:247, respectively. In contrast, the corresponding ratios within the Turn cascades are 357:241:218 and 631:331:247, respectively. Obviously, it shows that the enhancing tendencies of the single channel profile loss are mainly similar between the two groups, so the enhancements of boundary layer are mainly similar during the two highly-loaded designs. However, the Turn120 cascade shows much higher variating tendencies of the single channel endwall loss and $|\alpha_{3D,2}|-|\alpha_{2D,2}|$, so the enhancements of the Turn120 cascade should be much higher than the TCx150 cascade.

Table 2 The parameters for the verification of the load adjustment

		TCx150	TCx120	TCx100 (Turn90)	TCx083	TCx076	Turn120	Turn105	Turn75	Turn60
2D	$\delta\hat{m}_{2D}$	–0.40%	–0.61%	–	0.08%	–0.11%	–0.16%	–0.33%	–0.07%	–0.09%
	$\delta\|\alpha_{2D,2}\|$	0.12%	0.35%	–	–0.21%	–0.11%	–0.38%	0.08%	0.05%	0.07%
3D	Z_w	1.57	1.24	1.03	0.85	0.78	1.61	1.21	0.92	0.82
	C_o	0.95	0.81	0.71	0.61	0.58	0.96	0.79	0.65	0.59
	Ma_2	0.659	0.662	0.663	0.663	0.662	0.642	0.659	0.666	0.666
	Re_2	2.5×10^5	2.5×10^5	2.5×10^5	2.5×10^5	2.5×10^5	2.4×10^5	2.5×10^5	2.5×10^5	2.5×10^5
	$\delta\hat{m}_{3D}$	–0.40%	–0.71%	–	–0.26%	–0.40%	–1.16%	–0.08%	0.20%	0.42%
	$\delta\|\alpha_{3D,2}\|$	–0.89%	–0.32%	–	0.34%	0.40%	–2.87%	–0.35%	0.40%	0.52%

Table 3 The Parameters for evaluating the influence of the secondary flow

	TCx150	TCx120	TCx100 (Turn90)	TCx083	TCx076	Turn120	Turn105	Turn75	Turn60
ξ_{2D}	0.0239	0.0202	0.0218	0.0275	0.0293	0.0357	0.0241	0.0212	0.0209
ξ_{3D}	0.0564	0.0487	0.0465	0.0481	0.0497	0.0988	0.0572	0.0392	0.0382
$\xi_{3D}-\xi_{2D}$	0.0325	0.0285	0.0247	0.0206	0.0204	0.0631	0.0331	0.0180	0.0173
$\|\alpha_{3D,2}\|-\|\alpha_{2D,2}\|/(^\circ)$	–1.344	–1.143	–0.722	–0.382	–0.402	–2.213	–0.984	–0.505	–0.445

On considering the comparability between profiles shown in Section 3.1, it is reasonable to believe that the obvious unwanted disturbances such as large scale separations are avoided in highly-loaded design. Moreover, it is also proved in this section that the Turn120 cascade shows much stronger secondary flow than any other cascade in this study. Therefore, it should be reasonable to believe that the further strengthened secondary flow in the Turn120 cascade should be the main reason of its higher deviations in Table 2.

3.2.2 Comparative study based on 3D flow field

The energy loss coefficient is applied to analysis the influences of the highly-loaded designs on the secondary loss. Moreover, the Q criterion coefficient is also applied to ensure the variation of the flow structure, because it would be difficult to confirm the location of a vortex by ξ contours due to its low dissipation loss in some cases. Therefore, Fig. 6 presents the above to contours of the Turn cascades from $-0.10x_{Cx}$ plane to $1.1x_{Cx}$ plane, while the contours of the TCx cascades are present in Fig. 7. Moreover, the contours are transparent when ξ is less than 0.07.

Fig. 6 shows that the increased turning angle has enhanced the development of PV, CV, SV and the boundary layer near SS. Firstly, Fig. 6(b) shows the generating location of PV is moving towards the leading edge during the Turn highly-loaded design, while the locations of PV and SV are moving towards the midspan at the $1.10x_{Cx}$ plane. Therefore, the increased turning angle has accelerated the pitch-wise migration of PL-HV and enhanced the span-wise development of PV. Secondly, Fig. 6(a) shows the increased turning angle has led to obviously strengthened high-loss regions (increased range and core loss) near the midspan, so the development of the boundary layer near SS is enhanced by the Turn highly-loaded design. Thirdly, Fig. 6(a) shows the increased turning angle has also obviously strengthened (increased range and core loss) the high-loss regions of PV, CV and SV, so the developments of PV, CV and SV are also enhanced during the Turn highly-loaded design.

Fig. 7 shows that the increased cascade pitch has led to stronger PV, CV, SV and thicker boundary layer near SS, but the span-wise development of PV is weakened by the TCx highly-loaded design. Firstly, Fig. 7(b) shows the generating location of PV is moving towards the tailing edge during the TCx highly-loaded design, while the location of PV is moving towards the endwall at the $1.10x_{Cx}$ plane. Therefore, the increased cascade pitch has delayed the pitch-wise migration of PL-HV and suppressed the span-wise development of PV. Secondly, Fig. 7(a) shows the increased cascade pitch has obviously strengthened the high-loss regions (increased range and core loss) near the midspan, so the development of the boundary layer near SS is enhanced by the TCx highly-loaded design. Thirdly, Fig. 7(a) shows the

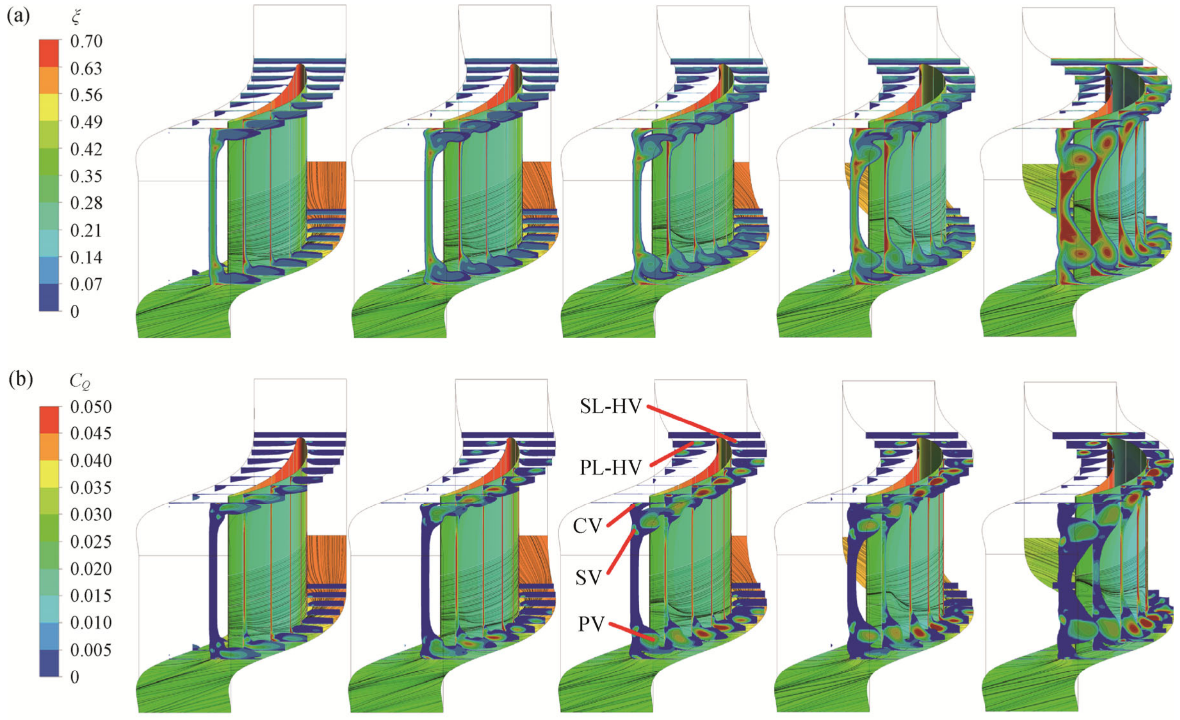

(a) Turn60   (b) Turn75   (c) Turn90   (d) Turn105   (e) Turn120

Fig. 6 Comparisons of the C_Q and ξ contours between the Turn cascades ($-0.10x_{Cx}$ to $1.10x_{Cx}$)

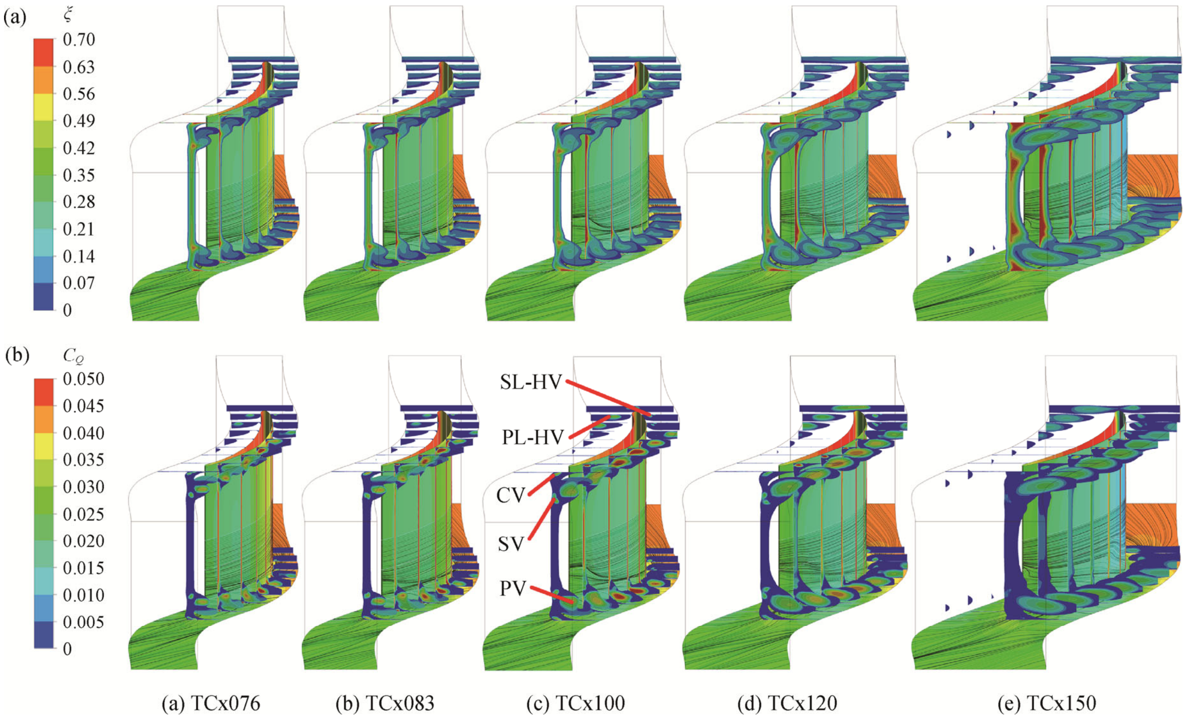

Fig. 7 Comparisons of C_Q and ξ contours the TCx cascades ($-0.10x_{Cx}$ to $1.10x_{Cx}$)

increased cascade pitch has obviously increased the ranges of the high-loss regions of PV, CV and SV, while the core losses of CV and SV are also obviously increased. Therefore, the developments of PV, CV and SV are all enhanced by the TCx highly-loaded design, but the enhancement of PV is limited because of its very slightly increased core loss.

According to the compassion between Fig. 6 and Fig. 7, it is clear that the two highly-loaded designs have both similar and different influences on the 3D flow field. Firstly, the two highly-loaded designs have both obviously enhanced the development of the boundary layer near SS, while the corresponding high-loss regions generally show similar enhancing tendencies. Secondly, the two highly-loaded designs have both obviously enhanced the developments of CV and SV, but the enhancements the high-loss regions in the Turn highly-loaded design are stronger than the TCx highly-loaded design. Thirdly, the two highly-loaded designs show different patterns in the enhancement of PV. In detail, the Turn highly-loaded design is enhancing the high-loss region of PV by obviously increasing its range and core loss at the same time, while the TCx highly-loaded design is enhancing the high-loss region of PV by obviously increasing its range and very slightly increasing its core loss.

Basing on the universal loss mechanism and flow structure that thoroughly studied by Denton [1] and Wang's team [2], detailed analyses about the flow field are carried out to analyze the enhancing mechanism and enhancing pattern of secondary flow. Fig. 8 presents the static pressure coefficient distributions at midspan of the cascades. The enhancements of the boundary layer near SS can be explained according to the figure, while the enhancements of vortexes can also be partly explained.

The variation of the static pressure coefficient on SS is the major change in each group, and it is also the major cause of the varied load. In detail, Fig. 8 shows that the two highly-loaded designs mainly cause significantly lower static pressure coefficients at the upstream side and the midstream side on SS, but slightly higher near the tailing edge on SS. In other words, the cascade load is mainly increasing at the upstream side and the midstream side on SS in each group, while the load distribution is moving forward. Therefore, the two highly-loaded designs both enhance the adverse pressure gradients, which would result in more unstable flow filed as well as thicker boundary layer, near SS.

Moreover, the strengthened deceleration tendency of fluid near SS would expand its migration time towards the tailing edge. Thus, the span-wise pressure gradient would show stronger influence because of the expanded action time, and the secondary migration tendency of the fluid would be directly enhanced. As a result, more low momentum fluid would participate in the secondary migration and accumulated on SS, while the enhanced accumulation would lead to more unstable flow field and stronger mixing progress in secondary flow structures. Therefore, the high-loss regions of the vortexes would be strengthened by the two highly-loaded designs.

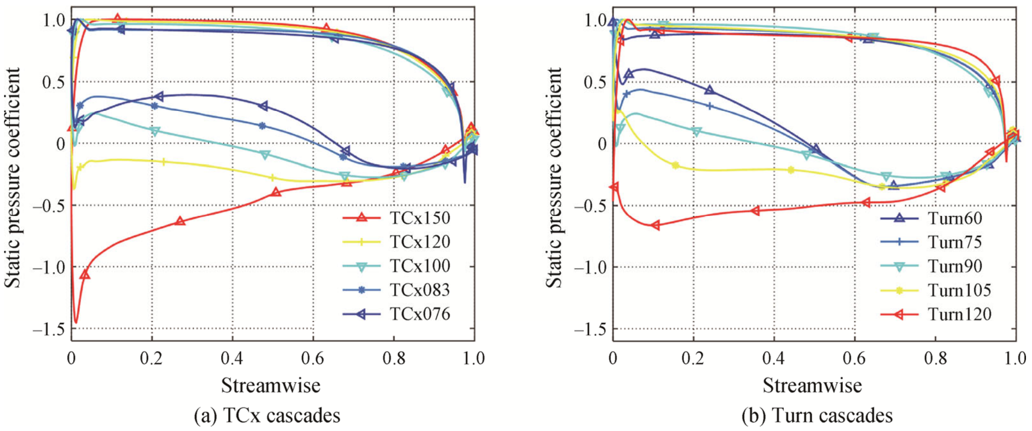

(a) TCx cascades (b) Turn cascades

Fig. 8 Comparisons of static pressure coefficient distributions at midspan

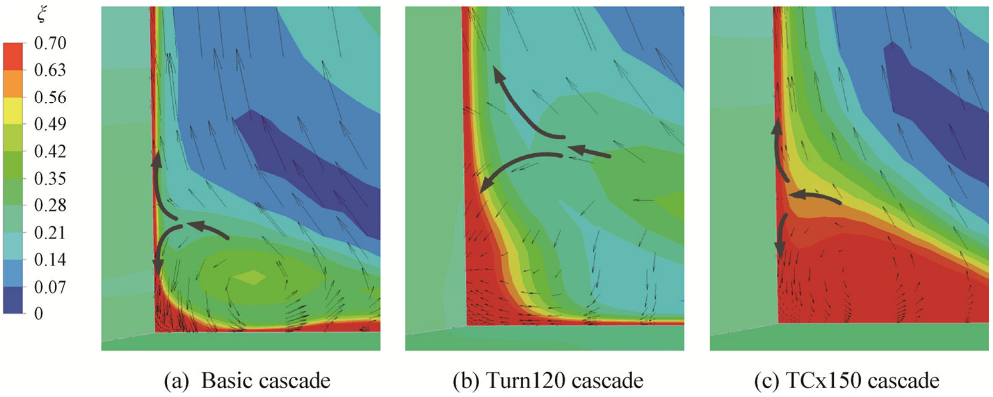

(a) Basic cascade (b) Turn120 cascade (c) TCx150 cascade

Fig. 9 A comparison of magnifications of the ξ contours and the projection of velocity vectors at $0.80x_{Cx}$ plane

Fig. 9 compares the magnifications of the ξ contours and the projection of velocity vectors at $0.80x_{Cx}$ plane between the Basic cascade and the two highest loaded cascades. Therefore, the interaction between the vortexes in the section-endwall corner could be directly presented; the enhancements of high-loss regions could be partly explained; and the immediate cause of the different enhancing patterns could be partly found out.

Generally, the flow fields in Fig. 9 are consistent with the Wang's secondary flow structure [2]. It shows that the cross flow is lifted away from the endwall because of the interaction between the accumulated low momentum fluid at the endwall-suction corner and the cross flow itself. Then, the cross flow reaches SS and is mainly divided into two streams towards the midspan and endwall, respectively. The cross flow would have strong interactions with low momentum fluid during deflection and span-wise migration, so it would enhance both the span-wise migration of low momentum fluid and the development of the vortexes. Therefore, the deflecting and span-wise migrating progresses would lead to expanded high-loss regions in the highly-loaded cascades because of the less stable flow field.

However, Fig. 9 shows that the deflecting progresses are different between the two highest loaded cascades. In detail, the increasing tendency of the span-wise velocity components and the reducing tendency of the pitch-wise velocity components near SS in the Turn120 cascade are both much stronger than the TCx150 cascade. Therefore, the deflecting progress of the cross flow should also be much stronger in the former than the latter, and this should be one of the directly causes of the different enhancing patterns.

3.3 Mechanism analysis of the different enhancing patterns

In this section, the different enhancing patterns of secondary flow would be discussed based on the both theoretical and numerical analysis.

3.3.1 Theoretical analysis of the pitch-wise pressure gradient

The following simplified derivation based on the Navier-Stokes equation proves that the variations of the cascade pitch and turning angle have different influences on the pitch-wise pressure gradient. Therefore, the two highly-loaded designs would have different influences on the development of HV and PV because the different pitch-wise migration variation trends of the fluid near endwall regions.

Taking a fluid element as the research object, the pitch-wise equation is described as follows:

$$\frac{\mathrm{d}v_y}{\mathrm{d}t}=f_y-\frac{1}{\rho}\frac{\partial p}{\partial y}+\upsilon\nabla^2 v_y \tag{9}$$

where $\frac{\mathrm{d}v_y}{\mathrm{d}t}$ is the pitch-wise acceleration; f_y is the pitch-wise mass force; $-\frac{1}{\rho}\frac{\partial p}{\partial y}$ is the pitch-wise pressure gradient, and $\upsilon\nabla^2 v_y$ is the pitch-wise viscous force.

When the fluid element is in the main-flow, the mass force and viscous force can be reasonably ignored in Eq. (9) to obtain:

$$\frac{\mathrm{d}v_y}{\mathrm{d}t}=-\frac{1}{\rho}\frac{\partial p}{\partial y} \tag{10}$$

Thus, from t_0 to t_1 it has:

$$\int_{t_0}^{t_1}\frac{\mathrm{d}v_y}{\mathrm{d}t}\mathrm{d}t=-\int_{t_0}^{t_1}\frac{1}{\rho}\frac{\partial p}{\partial y}\mathrm{d}t \tag{11}$$

If $\rho=f(p)$ and $P=\int\frac{\mathrm{d}p}{f(p)}$, we have $\frac{\partial P}{\partial y}=\frac{1}{\rho}\frac{\partial p}{\partial y}$. Thus, Eq. (11) can be converted to:

$$-\int_{t_0}^{t_1}\frac{\partial P}{\partial y}=v_{y,t_1}-v_{y,t_0} \tag{12}$$

If we define the equivalent constant of $\frac{\partial P}{\partial y}$ from t_0 to t_1 as $\frac{\partial\overline{P}}{\partial y}$, then Eq. (12) can be converted to:

$$-\frac{\partial\overline{P}}{\partial y}=\frac{v_{y,t_1}-v_{y,t_0}}{(t_1-t_0)} \tag{13}$$

When the equivalent constant of the channel width is defined as Y, the average pitch-wise pressure difference of the channel is:

$$\overline{P}=-\frac{v_{y,t_1}-v_{y,t_0}}{(t_1-t_0)}Y \tag{14}$$

It is reasonable to take t_1–t_0 as a constant because $\hat{m}$ and Cx are both approximately constant in this paper.

When the fluid element is in the boundary layer, only the mass force can be reasonably ignored in Eq. (9). Thus:

$$\frac{\mathrm{d}v_y}{\mathrm{d}t}=-\frac{1}{\rho}\frac{\partial p}{\partial y}+\upsilon\nabla^2 v_y \tag{15}$$

Taking the migration in y-z plane into consideration, Eq. (15) can be converted to:

$$\frac{\mathrm{d}v_y}{\mathrm{d}t}=-\frac{1}{\rho}\frac{\partial p}{\partial y}+\upsilon\left(\frac{\partial^2 v_y}{\partial y^2}+\frac{\partial^2 v_y}{\partial z^2}\right) \tag{16}$$

where $\frac{\partial^2 v_y}{\partial y^2}$ is the pitch-with velocity gradient and $\frac{\partial^2 v_y}{\partial z^2}$ is the span-wise velocity gradient. Because $\frac{\partial^2 v_y}{\partial y^2}\ll\frac{\partial^2 v_y}{\partial z^2}$ in the boundary layer, Eq. (16) can be converted to:

$$\frac{\mathrm{d}v_y}{\mathrm{d}t}=-\frac{1}{\rho}\frac{\partial p}{\partial y}+\upsilon\frac{\partial^2 v_y}{\partial z^2} \tag{17}$$

Thus, v_y would keep changing till $-\frac{1}{\rho}\frac{\partial p}{\partial y}$ was balanced by $\upsilon\frac{\partial^2 v_y}{\partial z^2}$ in the boundary layer.

According to Eqs. (13), (14) and (17), several qualitative conclusions can be summarized as follows:

(1) In theory, the turning angle has inevitably influence on the pitch-wise pressure gradient, because it would inevitably influence the variation of the pitch-wise velocity. Therefore, it is the increased pitch-wise pressure gradient that mainly increased the load in the Turn highly-loaded design.

(2) In theory, the cascade pitch has no inevitable connection with the variation of the pitch-wise pressure gradient, because it has no inevitable influence on the variation of the pitch-wise velocity. Therefore, it is the increased channel width that mainly increased the load in the TCx highly-loaded design.

(3) In theory, the two kinds of highly-loaded designs would show different influences on the cross flow because of the different influences on the pitch-wise pressure gradient and channel width. More specifically, increasing the turning angle would accelerate the development of cross flow and the generation of PV, while the increased cascade pitch would do the opposite.

(4) In theory, the enhancing patterns of the secondary flow should be more or less different between the two groups, and this situation should be taken into consideration in the improvement of the flow field.

3.3.2 Numerical validation and analysis

Therefore, the two highest loaded cascades would show the most obviously different enhancing patterns, which would be helpful in the validation of the theoretical analysis as well as the further analysis of the different patterns.

Fig. 10 compares the Cps and limiting streamlines on the endwall between the two highly-loaded cascades. It shows that the isobars are much denser along the pitch-wise direction in the Turn120 cascade than the TCx150 cascade. Besides, the separation line of PL-HV shows that HV might have not reached SS in the TCx150 cascade, while HV has reached SS at the upstream side of the channel in the Turn120 cascade.

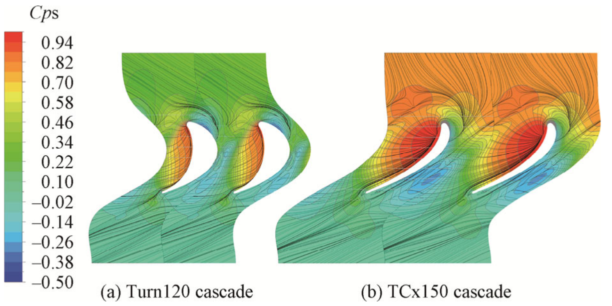

(a) Turn120 cascade (b) TCx150 cascade

Fig. 10 The limiting streamline and *Cps* distributions on the endwall

Therefore, the simulation result proves that the pitch-wise pressure gradient on the endwall and cross flow near the endwall are both much stronger in the Turn120 cascade than the TCx150 cascade, which is coincides well with Section 3.3.1.

Fig. 11 shows a schematic diagram of simplified PL-HV trajectories. Where O is the position of the saddle point, the MN lines are the normal of SS. Theoretically, the trajectory would move from OM_1 to OM_4 when the cross flow was delayed, while OM_1 and OM_3 are just tangent to the profile at M_1 and M_3, respectively. Therefore, the included angle between the vortex axis and the normal of SS (IAVS) is reducing from M_1 to M_2, and increasing from M_2 to M_3. After that, the OM lines would not contact with SS, while the delayed cross flow would lead to increased distance between the vortex and SS (DVS). For example, the length of M_4N' is the DVS of OM_4. Generally, the attaching location of PL-HV (M points) would rarely exist within the M_1-M_2 interval in highly-loaded cascades. Therefore, it is reasonable to suspect that the accelerated cross flow in the Turn highly-loaded design would lead to smaller IAVS or DVS, while the delayed cross flow in the TCx highly-loaded design would do the opposite.

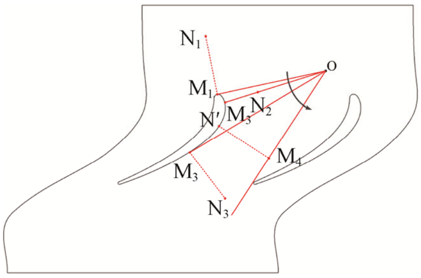

Fig. 11 A schematic diagram of different PL-HV trajectories

According to the study of Chester's team [45], it is obvious that the influences of the reduced IAVS or DVS in the Turn highly-loaded design would lead to stronger interaction between SS boundary layer and cross flow, while the increased IAVS or DVS in the TCx highly-loaded design would do the opposite. Therefore, the different deflecting progresses, which were discussed in Section 3.2.2 between the two highest loaded cascades, are reasonably explained by the theoretical and numerical analyses.

Moreover, the *Cps* distributions on SS and limiting streamlines on half of SS are presented in Fig. 12, so that the influences of the different deflecting progresses can be compared in detail. On one hand, the local high-pressure region near the attachment line of the cross flow and the span-wise pressure gradient nearby are both much stronger in the Turn120 cascade than the TCx150 cascade. Therefore, Fig. 12 proves that the enhancement of the interaction between the cross flow and the fluid near SS is much stronger in the Turn highly-loaded design than the TCx highly-loaded design. On the other hand, the limiting streamlines near the attachment line show much stronger span-wise deflecting tendencies the Turn120 cascade than the TCx150 cascade. Therefore, Fig. 12 proves that the enhancement of the span-wise migration near SS is also much stronger in the Turn highly-loaded design than the TCx highly-loaded design.

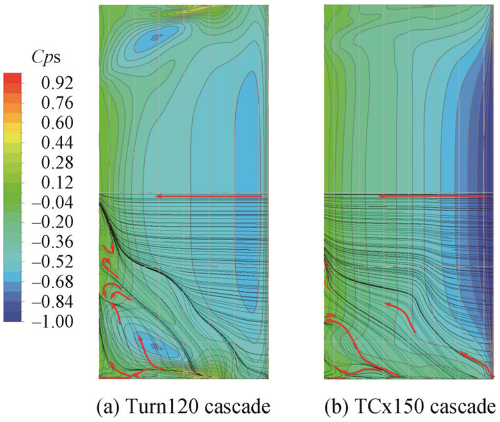

(a) Turn120 cascade (b) TCx150 cascade

Fig. 12 The *Cps* distributions on SS and limiting streamlines on half of SS

As a result, it shows that the varying tendency of the attaching location of PL-HV would be decided by the varying tendencies of the pitch-wise pressure gradient and channel width, while the different varying tendency of the attaching location would lead to different enhancing tendencies of the interaction between the cross flow and the fluid near SS. Therefore, it is reasonable that different enhancing patterns of the secondary flow would be shown between the Turn highly-loaded design and the TCx highly-loaded design.

4. Conclusions

The influences of the increased cascade pitch and turning angle were analyzed based on numerical simulations and theoretical derivations in this paper. The mechanisms of the enhanced secondary flow as well as the different enhancing patterns were both studied and conclusions are drawn as following:

(1) The two highly-loaded designs have different load enhancing mechanisms. In theory, the pitch-wise pressure gradient would be inevitably influenced only by the variation of the pitch-wise velocity in this study. Thus, the increased load in the Turn highly-loaded design is mainly caused by the strengthened pitch-wise pressure gradient, while in the TCx highly-loaded design it is mainly caused by the increased channel width.

(2) The similarly enhanced adverse pressure gradient and span-wise gradient near SS are the main reason of the similar secondary flow enhancing patterns between the two highly-loaded designs. The strengthened adverse pressure gradient would weaken the flow filed stability. Therefore, the strengthened span-wise gradient would enhance the span-wise migrating and accumulating tendencies of the low-momentum fluid. As a result, the two highly-loaded designs both lead to thicker boundary layers and stronger vortexes.

(3) The different enhancing patterns of the secondary flow are fundamentally caused by the different load enhancing mechanisms between the two highly-loaded designs. The different load increasing mechanisms show different influences on the pitch-wise migrating tendency of the cross flow. In detail, the strengthened pitch-wise pressure gradient would accelerate the cross flow in the Turn highly-loaded design, while the increased channel width in the TCx highly-loaded design would delay the cross flow. Then, the varying tendency of the attaching location of PL-HV, or to say the varying tendencies of IAVS or DVS, would obviously influences the interaction between the cross flow and the fluid near SS. Therefore, different enhancing patterns of the secondary flow would be shown between the Turn highly-loaded design and the TCx highly-loaded design. More specifically, the span-wise developments of CV, SV and PV near SS would have much stronger enhancing tendencies in the Turn highly-loaded design than the TCx highly-loaded design.

References

[1] Denton J.D., The 1993 IGTI scholar lecture: Loss mechanisms in turbomachines. Journal of Turbomachinery, 1993, 115(4): 621–656.

[2] Wang H.P., Olson S.J., Goldstein R.J., Eckert E.R.G., Flow visualization in a linear turbine cascade of high performance turbine blades. Journal of Turbomachinery, 1997, 119(1): 1–8.

[3] Langston L.S., Secondary flows in axial turbines—A review. Annals of the New York Academy of Sciences, 2001, 934(1): 11–26.

[4] Cui J., Rao V.N., Tucker P.G., Numerical investigation of secondary flows in a high-lift low pressure turbine. International Journal of Heat and Fluid Flow, 2017, 63: 149–157.

[5] Kan X.X., Wang S.T., Luo L., Su J.X., Investigation of optimizing a compressor cascade with curved blade based on the weight distribution of flow losses. Journal of Engineering Thermophysics, 2018, 39: 504–512.

[6] Prakash C., Cherry D.G., Shin H.W., Machnaim J., Dailey L., Beacock R., Halstead D., Wadia A.R., Effect of loading level and distribution on LPT losses. ASME Turbo Expo 2008: Power for Land, Sea, and Air, Berlin, Germany, 2008, 6: 917–925.
DOI: 10.1115/GT2008-50052.

[7] Howell R.J., Hodson H.P., Schulte V., Schiffer H., Haselbach F., Harvey N.W., Boundary layer development in the BR710 and BR715 LP turbines: The implementation of high-lift and ultra-high-lift concepts. Journal of Turbomachinery, 2002, 124(3): 385–392.

[8] Chen S.W., Zhou Z.H., Wang S.T., Wang Z.Q., Numerical investigation of boundary layer suction on certain highly loaded aspirated compressor at low speeds cascade. Proceedings of the Institution of Mechanical Engineers, Part G: Journal of Aerospace Engineering, 2018, 232(1): 30–41.

[9] Moustapha S.H., Paron G.J., Wade J.H.T., Secondary flows in cascades of highly loaded turbine blades. Journal of Engineering for Gas Turbines and Power, 1985, 107(4): 1031–1038.

[10] Qu X., Zhang Y.F., Lu X.E., Lei Z.J., Zhu J.Q., The effect of endwall boundary layer and incoming wakes on secondary flow in a high-lift low-pressure turbine cascade at low Reynolds number. Proceedings of the Institution of Mechanical Engineers, Part G: Journal of Aerospace Engineering, 2019, 233(15): 5637–5649.

[11] Coull J.D. Endwall loss in turbine cascades. Journal of Turbomachinery, 2017, 139(8): 081004.

[12] Tan C.Q., Zhang H.L., Xia H.D., Chen H.S., Blade bowing effect on aerodynamic performance of a highly loaded turbine cascade. Journal of Propulsion and Power, 2010, 26(3): 604–608.

[13] Chen S.W., Chen F., Wang K.L., Gu J., Wang Z.Q., Aerodynamic performance study of curved compressor cascades with different camber angles. Journal of Propulsion Technology, 2007, 28(2): 170–175.

[14] Ingram G., Gregory-Smith D., Harvey N., Investigation of a novel secondary flow feature in a turbine cascade with end wall profiling. Journal of Turbomachinery, 2005, 127(1): 209–214.

[15] Weiss A.P., Fottner L., The influence of load distribution on secondary flow in straight turbine cascades. Journal of Turbomachinery, 1995, 117(1): 133–141.

[16] Lyall M.E., Effects of front-loading and stagger angle on endwall losses of high lift low pressure turbine vanes. Air Force Institute of Technology, Ohio, USA, 2012.

[17] Lyall M.E., King P.I., Clark J.P., Sondergaard R., Endwall loss reduction of high lift low pressure turbine airfoils using profile contouring—Part I: Airfoil design. Journal of Turbomachinery, 2014, 136(8): 081005.

[18] Sangston K., Little J., Lyall M.E., Sondergaard R., Effect of blade profile contouring on endwall flow structure in a high-lift low-pressure turbine cascade. Journal of Turbomachinery, 2016, 139(2): 021006.

[19] Tsujita H., Yamamoto A., Influences of incidence angle on 2D-flow and secondary flow structure in ultra-highly loaded turbine cascade. Journal of Thermal Science, 2014, 23(1): 13–21.

[20] Taylor J.V., Miller R.J., Competing three-dimensional mechanisms in compressor flows. Journal of Turbomachinery, 2016, 139(2): 021009.

[21] Goldstein R.J., Spores R.A., Turbulent transport on the endwall in the region between adjacent turbine blades. Journal of Heat Transfer, 1988, 110(4a): 862–869.

[22] Zess G.A., Thole K.A., Computational design and experimental evaluation of using a leading edge fillet on a gas turbine vane. Journal of Turbomachinery, 2002, 124(2): 167–175.

[23] Sangston K., Little J., Lyall M.E., Sondergaard R., End wall loss reduction of high lift low pressure turbine airfoils using profile contouring—Part II: Validation. Journal of Turbomachinery, 2014, 136(8): 081006.

[24] Ingram G., Gregory-Smith D., Rose M., Harvey N., Brennan G., The effect of end-wall profiling on secondary flow and loss development in a turbine cascade. ASME Turbo Expo 2002: Power for Land, Sea, and Air, Amsterdam, Netherlands, 2002, 5: 135–145. DOI: 10.1115/GT2002-30339.

[25] Torre D., Vázquez R., Blanco E.D.L.R., Hodson H.P., A new alternative for reduction in secondary flows in low pressure turbines. Journal of Turbomachinery, 2010, 133(1): 011029.

[26] Tan C.Q., Yamamoto A., Mizuki S., Chen H.S., Influences of blade bowing on flow fields of turbine stator cascades. AIAA Journal, 2003, 41(10): 1967–1972.

[27] Han W.J., Wang Z.Q., Tan C.Q., Shi H., Wang Z.Q., Effects of leaning and curving of blades with high turning angles on the aerodynamic characteristics of turbine rectangular cascades. Journal of Turbomachinery, 1994, 116(3): 417–424.

[28] Xue X.X., Wang S.T., Luo L., Zhou X., The compound bowing design in a highly loaded linear cascade with large turning angle. Proceedings of the Institution of Mechanical Engineers Part G-Journal of Aerospace Engineering, 2020, 234(16): 2323–2336.

[29] Zweifel O., The spacing of turbo-machine blading, especially with large angular deflection. Brown Boveri Review, 1945, 32(12): 436–444.

[30] Bear P., Wolff M., Gross A., Marks C.R., Sondergaard R., Experimental investigation of total pressure loss development in a highly loaded low-pressure turbine cascade. Journal of Turbomachinery, 2017, 140(3): 031003.

[31] Coull J.D., Hodson H.P., Blade loading and its application in the mean-line design of low pressure turbines. Journal of Turbomachinery, 2013, 135(2): 021032.

[32] Hunt J.C.R., Wray A., Moin P., Eddies, stream and convergence zones in turbulent flows. Studying Turbulence Using Numerical Simulation Databases: Proceedings of the 1988 Summer Program, 1988, California, USA, 19890015184.

[33] Haller G., An objective definition of a vortex. Journal of Fluid Mechanics, 2005, 525: 1–26.

[34] ANSYS CFX. Reference Guide, Relaease 15, 2013.

[35] Wang W.H., Lu Z.H., Deng K.Y., Qu S., An experimental study of compressible combining flow at 45° T-junctions. Proceedings of the Institution of Mechanical Engineers, Part C: Journal of Mechanical Engineering Science, 2015, 229(9): 1600–1610.

[36] Kurz J., Hoeger M., Niehuis R., Active boundary layer control on a highly loaded turbine exit case profile. International Journal of Turbomachinery, Propulsion and Power, 2018, 3(8): 1–14.

[37] Zhong J.J., An experimental investigation by using curved blade to control secondary flow in compressor cascade. Harbin Institute of Technology, Heilongjiang, China, 1996.

[38] Ling J., Study of the influence of cascade parameters on curved blade loss and deviation in compressor cascade. Harbin Institute of Technology, Heilongjiang, China, 2015.

[39] Bardera R., Meseguer J., Flow in the near air wake of a modified frigate. Proceedings of the Institution of Mechanical Engineers, Part G: Journal of Aerospace Engineering, 2015, 229(6): 1003–1012.

[40] Hao Y., Liu Y.W., Li Q.S., Lu L.P., Turbulence characteristics in corner separation in a highly loaded linear compressor cascade. Aerospace Science and Technology, 2018, 75: 139–154.

[41] Amiralaei M.R., Alighanbari H., Hashemi S.M., Numerical modelling of a low Reynolds number plunging airfoil flow field characteristics. Proceedings of the Institution of Mechanical Engineers, Part G: Journal of

Aerospace Engineering, 2013, 227(8): 1251–1264.

[42] Xu W.J., Du X., Wang S.T., Wang Z.Q., Correlation of solidity and curved blade in compressor cascade design. Applied Thermal Engineering, 2018, 131: 244–259.

[43] Blanco E.R.D.L., Hodson H.P., Vazquez R., Torre D., Influence of the state of the inlet endwall boundary layer on the interaction between pressure surface separation and endwall flows. Proceedings of the Institution of Mechanical Engineers, Part A: Journal of Power and Energy, 2003, 217(4): 433–441.

[44] Xue X.X., Zhou X., Liu X., Wen F.B., Investigation on pitch-wise non-uniform and inflecting inlet flow of low-speed plane cascade. ASME Turbo Expo 2016: Turbomachinery Technical Conference and Exposition, Seoul, South Korea, 2016, V02AT37A028. DOI: 10.1115/GT2016-56934.

[45] Chester N.L., Wells M.A., Prodanovic V., Effect of inclination angle and flow rate on the heat transfer during bottom jet cooling of a steel plate. Journal of Heat Transfer, 2012, 134(12): 122201.